Ultrasonics 131 (2023) 106939

Contents lists available at ScienceDirect

Ultrasonics

journal homepage: www.elsevier.com/locate/ultras

Stiffness tensor estimation of anisotropic crystal using point contact method and unscented Kalman filter

Nur M.M. Kalimullah [a], Kaushik Shukla [b], Amit Shelke [a,*], Anowarul Habib [c,*]

[a] Department of Civil Engineering, Indian Institute of Technology Guwahati, Assam 781039, India
[b] Department of Electronics Engineering, Indian Institute of Technology (Indian School of Mines) Dhanbad, Jharkhand 826004, India
[c] Department of Physics and Technology, UiT The Arctic University of Norway, 9037 Tromsø, Norway

ARTICLE INFO

Keywords:
Anisotropy
Coulomb coupling
Kalman filter
Lithium Niobate
Parameter estimation

ABSTRACT

The potential application of Lithium Niobate ($LiNbO_3$) crystal is immense, specifically in the domain of *meta*-surfaces and nano-resonators. However, the practical application of $LiNbO_3$ is impeded due to unreliable experimental techniques and inaccurate inversion algorithms for material characterization. In the current research, material characterization of anisotropic crystal is proposed by exploring the wavefield evolution in the spatial and temporal domains. The presented framework has three major components: a physics-based mathematical model (Christoffel equation), a novel experimental technique, and an inversion algorithm based on Bayesian filtering. An experimental technique based on Coulomb coupling is devised to visualize the propagation of ultrasonic waves in an anisotropic crystal. The crystal is characterized by measuring the directional-dependent acoustic wave velocity from the spatial–temporal information of the wave propagation. The anisotropic constitutive properties of the crystal are estimated by exploring the wave velocity in the Bayesian filtering algorithm. The proposed algorithm is based on the probabilistic framework that integrates the experimental measurement in a physics-based mathematical model for optimal state prediction of stiffness tensor through the Bayesian filtering algorithm. In particular, we utilize the unscented Kalman filter (UKF) in conjunction with the plane-wave Eigen solution to estimate the constitutive parameters. In the presence of measurement uncertainties, the performance of the optimal prediction algorithm is illustrated by comparing the estimated parameter with the corresponding theoretical value. The comparison demonstrates that the proposed inversion algorithm is efficient and robust and performs satisfactorily even with significant measurement uncertainties.

1. Introduction

Lithium Niobate ($LiNbO_3$) is a piezoelectric crystal that is extensively used in optical and acoustic applications due to its operational broadband frequency and high piezoelectric coupling coefficient [1,2]. Recently $LiNbO_3$ has shown promising capabilities for its application in nanoscale integrated optics [3], high-Q micro acoustic resonators [4,5], optoacoustic circuits [6], fast electro-acoustic- optical modulators [7,8], and high-frequency waveguides [9,10]. These excellent features are attributed to higher second-order optical-acoustic nonlinearity with low losses in the broadband spectrum [11,12]. Despite the fact that $LiNbO_3$ has the inherent potential to control and modulate non-linear optical and acoustic generation, it is still in the nascent stage for practical application in domains of metasurfaces, nano-resonators and acoustic phononic crystals. One of the reasons attributed to the limited use of $LiNbO_3$ in the area of nanophotonic application is the lack of reliable experimental investigation for material characterization at the micro-scale. Moreover, the estimation of the constitutive stiffness tensor of $LiNbO_3$ is unreliable due to the poor performance of the inversion algorithm in the presence of experimental inaccuracies and uncertainties.

In the last several decades, the visualization of bulk acoustic and surface acoustic waves (SAWs) in the anisotropic piezoelectric crystal has been an active area of research [13–15]. The generation and detection of bulk waves and SAWs in piezoelectric crystals with the aid of an inter-digital transducer (IDT) have attracted widespread scientific interest for signal processing and filtering applications [16–18]. A wide range of experimental investigations on SAWs were implemented to detect and visualize the SAW field, such as stroboscopic X-ray topography and photoemission electron microscopy [19,20], scanning acoustic force electron microscopy [21], immersed focusing transducers

* Corresponding authors.
E-mail addresses: amitsh@iitg.ac.in (A. Shelke), anowarul.habib@uit.no (A. Habib).

https://doi.org/10.1016/j.ultras.2023.106939
Received 6 April 2022; Received in revised form 23 January 2023; Accepted 26 January 2023
Available online 2 February 2023

[22], scanning electron microscopy [23], neutron scattering [24], and optical detection [25]. Notable contribution for generating elastic strain waves by thermal expansion of phonon using ultra-short (picosecond) light pulse technique has gained significant attention [25–28]. These strain pulses produce a coherent pulse with longitudinal polarisation bulk acoustic waves in the crystal [26,27]. Wolfe (2005) has devised a picosecond photoluminescence imaging technique with Laser excitation producing a localized source of thermal energy exciting quantized lattice vibration [29]. The developed technique was capable of excitation and detection of bulk waves, SAWs and phonons focusing on low temperatures in the crystals. A similar technique was developed by Sugawara, et al. (2002) for studying the longitudinal polarised bulk and skimming surface phonon focusing pattern in piezoelectric crystals [30]. The heat pulse technique relies on the complete understanding of the interaction of thermal gradient with phonon vibration at variable temperatures. Moreover, certain materials that are sensitive to thermal excitation are not ideally suited for material characterization using the pulse heating technique. Grill, et al. (1996) have developed a point-focusing ultrasound lens for the excitation and detection of longitudinal and transversal bulk waves in anisotropic crystals [31]. However, the focusing ultrasound lens suffers from reverberation due to multiple reflections within the lens and causing interference with the waves. This reverberation leads to a complicated wave pattern. Experimentally and theoretically, the phenomena of phonon focusing in anisotropic crystals have been illustrated in detail [29,32]. Every, et al. (2004) have theoretically studied the development of bulk waves and phonon caustics and its unfolding into characteristic differ patterns through the angular spectrum technique [33]. However, the real-time imaging of the bulk waves, SAWs and Lamb waves over distances larger than the characteristic length are absent in the literature. Recently, our research group has developed a local electric field probe technique for visualizing the propagation of bulk waves and SAWs in anisotropic materials [34] by overcoming the limitation mentioned in the aforementioned techniques.

Point contact excitation and detection scheme based on Coulomb coupling has been studied for visualization of ultrasonic waves in piezoelectric crystals [13]. The Coulomb coupling excites harmonic and subharmonic waves that demonstrate several interesting phenomena of acoustic waves propagation in isotropic/anisotropic crystal, such as internal diffraction, phonon focusing, mode conversion due to detecting interaction and the metamorphosis of the bulk wave to Lamb wave [14,15]. In the anisotropic piezoelectric crystal, the directional evolution of polarised acoustic wave is a function of elastic constitutive tensor. The generalized Christoffel equation provided directional phase velocities and polarisation of bulk wave in the direction normal "**n**" by computing the Eigen decomposition of constitutive tensor [32,35]. The inversion of the Christoffel equation to recover elastic constitutive tensor from measured direction wave velocities are sparse in literature [36].

Based on the experimental investigation, the challenge is to develop a robust inversion algorithm to extract the constitutive properties of fully anisotropic ceramics. Cui and di Scalea (2019) have used the Simulated Annealing (SA) optimization algorithm and Semi-Analytical Finite Element (SAFE) method to identify the elastic properties of composite materials using guided wave mode [37]. Balasubramaniam (1998) used a phase velocity dispersion curve, and Genetic Algorithm (GA) based optimization technique to identify the material properties [38]. Recently, Chen, et al. (2021) used a similar approach to estimate the elastic constants of the isotropic and transversely isotropic plates [39]. It is reported that the high-resolution dispersion curve of Lamb wave and constitutive properties of the material were estimated by employing the estimation of signal parameters via the rotation invariant technique (ESPRIT) followed by particle swarm optimization (PSO). These techniques employed various global optimization schemes as an inversion algorithm may not always guarantee the global optimum. Rautela, et al. (2020), Gopalakrishnan, et al. (2020) have utilized a learning-based technique to calculate the material properties [40,41]. They trained a supervised deep neural network (DNN) with ultrasonic-guided wave modes as input and estimated the elastic properties through a neural network model. However, a significant number of labelled datasets is required to train such a network to achieve sufficient accuracy. Further, the above-mentioned research works do not incorporate any uncertainties arising from experimental observations. The strategies based on the time of flight (TOF) measurements are often used to compute the velocity field of the propagated wave [42,43]. Further, in TOF-based strategies, the accuracy of TOF measurement is crucial as the erroneous measurement will lead to a considerable error in the estimation of the elastic constants. Generally, the sources of error that arise are dispersion phenomena, mode change, interaction with boundaries and defects, noise, temperature variations, and systematic error, to mention a few [44].

On the contrary, the data assimilation techniques such as Kalman Filter (KF), Ensemble Kalman Filter (EnKF), Particle Filter (PF), and Hierarchical Bayesian Method (HBM) based on the probabilistic framework highlights the importance of statistical uncertainties in the estimation of system parameters [45–47]. The fact is, in a real-life scenario, the measurements and hybrid simulations are significantly affected by noise and/or uncertainties. However, data assimilation techniques optimally estimate the parameters by fusing the physics-based model with the measurements available from the field experiment. Data assimilation is conceivably-one of the most useful data-driven techniques that make optimal use of measurement and numerical models.

Lithium Niobate is an anisotropic single crystal most preferable for photonic, electronic and sensor applications. It has been extensively employed in optical fibres, optical modulators, beam deflectors and thin film photonic devices. In these applications, various cuts of Lithium Niobate are used. Further, the accurate and complete characterisation of the material is essential prior to the usage of the substrate. The piezoelectric substrates are characterised by elastic, piezoelectric, and dielectric material constants. However, the challenge is that crystal growth and chemical composition can largely change the acoustical physical constants compared to the initial stage of the research and development, which can change the velocity of the bulk and guided waves. The main thrust of this study is to develop a robust and reliable framework that can estimate the constitutive parameters of the crystal from the noisy/uncertain velocity profile. We would like to remark that the proposed framework is generic that can be extended to estimate the constitutive parameters of any other anisotropic material.

A novel approach based on a non-linear Bayesian filter is proposed to estimate the constitutive tensor of anisotropic $LiNbO_3$ crystal from wavefield imaging to address the aforementioned research gaps. Point contact excitation and detection scheme is explored for visualization of the acoustic wave in piezoelectric crystal. One must note that the proposed procedure is modular, so different experimental techniques can also be used to create the measurement dataset. The Bayesian filter is a probabilistic framework; hence it provides a confidence interval of the estimated parameters, which gives an advantage in decision-making. Kalman filter is one of the Bayesian filtering techniques widely accepted in many engineering disciplines, such as climate prediction, spacecraft tracking, and localization of acoustic source emission [45,48–50]. In this paper, we used an unscented Kalman filter among the Bayesian filter available in the literature. The Kalman filtering framework requires a set of physics-based equations and measurement equation that depicts the real-world model.

In the current context, if the constitutive parameter describes the state of a system, then the Christoffel equation can be considered the measurement equation that relates the state to the measurement. However, in practice, these physics-based mathematical equations alone do not prescribe the real-world model accurately. For a highly non-linear system that is prevalent in a real-world case, a small perturbation of noise and/or uncertainties can lead to significant changes in the system's behaviour, stability, and predictability. Kalman filtering is a

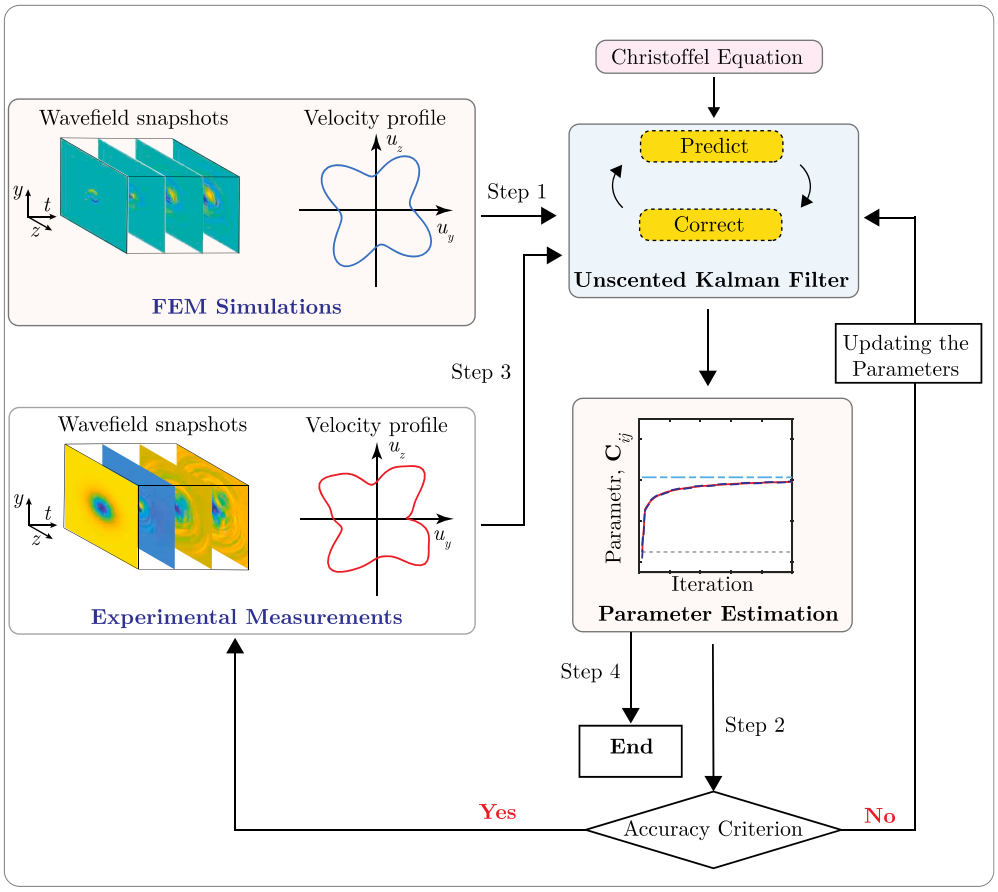

Fig. 1. The general approach for constitutive parameter estimation, emphasizing the unscented Kalman filter framework.

technique that attempts to mitigate the effect of noise and uncertainties present in the system. The main thrust of the current research is to develop a unified framework for the parameter estimation of the stiffness tensor of the piezoelectric material. The idea is to utilize the measurement information, such as the velocity of ultrasonic waves and integrate it with the numerical model prediction to better estimate the constitutive parameters. Prior to that, the framework of the algorithm is calibrated and verified with the FEM simulation data. The current work conceives the experimental technique using a local electric field probe in conjunction with the Bayesian filter for the estimation of the constitutive parameters of an anisotropic piezoelectric material. The schematic representation of the overview of the paper accentuating the constitutive parameter estimation framework based on the unscented Kalman filter is shown in Fig. 1.

2. Finite element method simulation

The main aim of conducting numerical finite element method (FEM) analysis is to generate angular velocity maps for anisotropic solids, which further be used for calibration of the proposed UKF algorithm. The accuracy and efficacy of the UKF algorithm for parameter estimation of Lithium Niobate crystal is benchmarked using FEM velocity profile results. The FEM is widely used to simulate ultrasonic wave propagation in an anisotropic substrate. The simulation parameters, such as material properties and excitation waveform, play a significant role in the visualization of transient wave propagation and the modal analysis of waves.

In piezoelectric materials, acoustic wave propagation is governed by two systems of equations; (i) the mechanical equation of motion and (ii) Maxwell's equation for electric behaviour. The constitutive characteristics of piezoelectric materials couple these two systems of equations in the elastic range of the material.

$$\begin{aligned} T_{ij} &= C_{ijkl}S_{kl} - e_{kij}E_k \\ D_i &= e_{ikl}S_{kl} + \varepsilon_{ik}E_k \end{aligned} \tag{1}$$

where, T_{ij} are the stress components, C_{ijkl} the elastic constant, S_{kl} the strain, E_k the electric field intensity, e_{ikl} the piezoelectric constant, and ε_{ik} the permeability. In typical piezoelectric substrates, the acoustic wave propagates five times slower than the electromagnetic waves. Hence, one can assume the piezoelectric coupled field as quasistatic. Therefore, Maxwell's equations can be reduced to

$$\frac{\partial D_i}{\partial x_i} = 0 \tag{2}$$

and

$$E_i = -\frac{\partial \varphi}{\partial x_i} \tag{3}$$

where, D_i are the electric field displacement components and φ the electric field potential. The electric charge inside the piezoelectric substrate is assumed to be zero because the substrates are supposed to be perfect insulators. The equation of motion can be expressed in the absence of internal body force as

$$\frac{\partial T_{ij}}{\partial x_j} - \rho\frac{\partial^2 u_i}{\partial t^2} = 0 \tag{4}$$

where, ρ is the density of the medium and u_i are the displacement field components. Further, one can define the components of strain as

$$S_{ij} = \frac{1}{2}\left(\frac{\partial u_i}{\partial x_j} + \frac{\partial u_j}{\partial x_i}\right) \tag{5}$$

Now, substituting the Eqs. (3) and (5) into Eq. (1) and hence Eqs. (2)

Table 1
Value of the constitutive parameters of the $LiNbO_3$ crystal.

Materials	Stiffness (10^{10}N/m^2)					Density, ρ (kg/m^3)
	C_{11}	C_{13}	C_{14}	C_{33}	C_{44}	
Lithium Niobate	20.3	7.5	0.9	24.5	6	4700

and (4) results in a system of coupled wave equations for the electric potential and displacement in piezoelectric substrates,

$$-\rho\frac{\partial^2 u_i}{\partial t^2}+C_{ijkl}\frac{\partial^2 u_k}{\partial x_j\partial x_l}+e_{kij}\frac{\partial^2\varphi}{\partial x_k\partial x_j}=0$$
$$e_{ikl}\frac{\partial^2 u_k}{\partial x_i\partial x_l}-\varepsilon_{ik}\frac{\partial^2\varphi}{\partial x_i\partial x_k}=0. \tag{6}$$

Conveniently these equations are solved using finite element analysis. In this work, 3D FEM simulation of ultrasonic wave in the time domain is conducted in an anisotropic $LiNbO_3$ crystal using commercially available FEM solver COMSOL Multiphysics 5.6 version. The simulated geometry considered here is 8 mm × 8 mm X-cut $LiNbO_3$ substrate having a thickness of300 μm. Table 1 presents the mean theoretical value of the constitutive parameter of $LiNbO_3$ crystal [32]. The piezoelectricity physics is added under the electromagnetic structure interaction menu available in the physics tab of the COMSOL Multiphysics program. This adds both Physics nodes and Multiphysics nodes. Under the physics nodes, the Solid Mechanics and Electrostatics effects are added, and the Piezoelectric effect is considered under the Multiphysics coupling node. In Solid Mechanics physics, the low reflecting boundary condition is applied at all edges along the bottom boundary to absorb the outgoing waves. Thus, no reflection occurs, and interference among the waves can be avoided. The electrostatic potential and ground boundary conditions are added at the top and bottom flat surfaces under the Electrostatics physics. The time-dependent equations are solved for the low-reflecting boundary given in Eq. (7).

$$\sigma\cdot\boldsymbol{n}=-\boldsymbol{d}_{\mathrm{im}}(\rho,c_s,c_p)\frac{\partial\boldsymbol{u}}{\partial t} \tag{7}$$

where, $\boldsymbol{n}$ is the unit normal vector at the boundary, c_s and c_p are the speeds of pressure and shear waves respectively, and $\boldsymbol{d}_{\mathrm{im}}$ is the mechanical impedance matrix.

$$\boldsymbol{d}_{\mathrm{im}}=\rho\frac{c_p+c_s}{2}\boldsymbol{I} \tag{8}$$

where, $\boldsymbol{I}$ is the identity matrix.

The excitation rectangular pulse of 20 ns width at an input voltage of 10 V is employed as an input excitation signal. The mesh is generated with tetrahedral elements. To avoid numerical instability, the integration time step (Δt) was selected as$\Delta t = {}^{1}/_{20f_{\max}}$, where $f_{\max}$ is the maximum frequency that controls the integration time step and element size. The maximum element size employed in the simulation is less than$\lambda/5$, which corresponds to, five mesh elements per wavelength. Here, λ is the shortest wavelength of the ultrasonic wave. However, for the convergence study, the maximum mesh element size is kept as$\lambda/factor$, where the *factor* at denominator is varied from 1 to 5, corresponding to 1 to 5 mesh elements per wavelength. To investigate the convergence properties of the FEM model, two metrics are considered: (i) the absolute maximum displacement of the output displacement signal and (ii) The absolute difference of the energy content in the output signal. The maximum displacement along the perpendicular direction of the substrate plane at an arbitrarily chosen point (0, 1, 1) is illustrated in Fig. 2(a). This can be observed that the result converges for a *factor* value of more than 2. Fig. 2(b) illustrates the absolute difference of the energy content in the output time-domain displacement signals for two consecutive mesh element sizes. The outputs are taken from 10 arbitrarily chosen points on the FEM model for the various mesh element sizes. The blue bar in Fig. 2(b) depicts the $\mu \pm \sigma$ where μ is average value and σ is the standard deviation of the ten samples considered in the study. For instance, $E(\lambda/3)$ indicates the energy of the output signal corresponding to the mesh element size of$\lambda/3$. Note that the energy difference approaches zero($|E(\lambda/5)-E(\lambda/4)|\rightarrow 0$), that indicates the model converges with sufficient accuracy for the mesh element size of$\lambda/5$. In the simulation, time-dependent analysis and time-dependent solver are used for the solution. The directional-dependent velocity profile is extracted and used for UKF code calibration, as discussed in Section 6.3.

3. Experimental technique

Our group has already presented an extensive overview of the excitation and detection probes fabrication as well as the experimental setup [13,51–53]. Fig. 3 shows the schematic diagram of the local electric field probe for excitation and detection of ultrasonic waves in piezoelectric crystal.

Two motor-driven translation stages were used in order to position the probe and for time-synchronized excitation of ultrasonic waves on

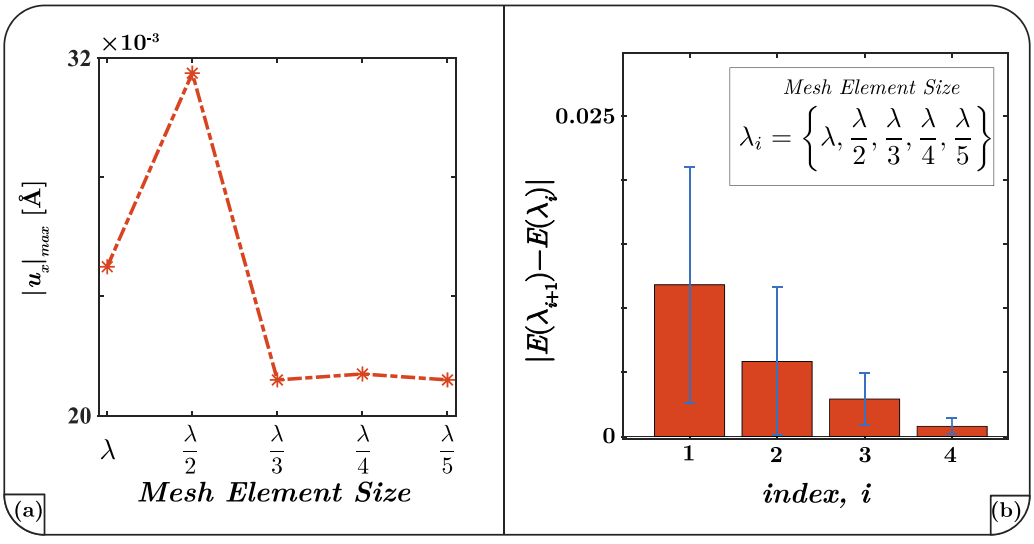

Fig. 2. Illustration of the convergence of the finite element model for various mesh element sizes, (a) variation of absolute maximum displacement with respect to the different mesh element sizes, and (b) absolute difference of the energy content in the time domain output signal between two consecutive mesh element sizes.

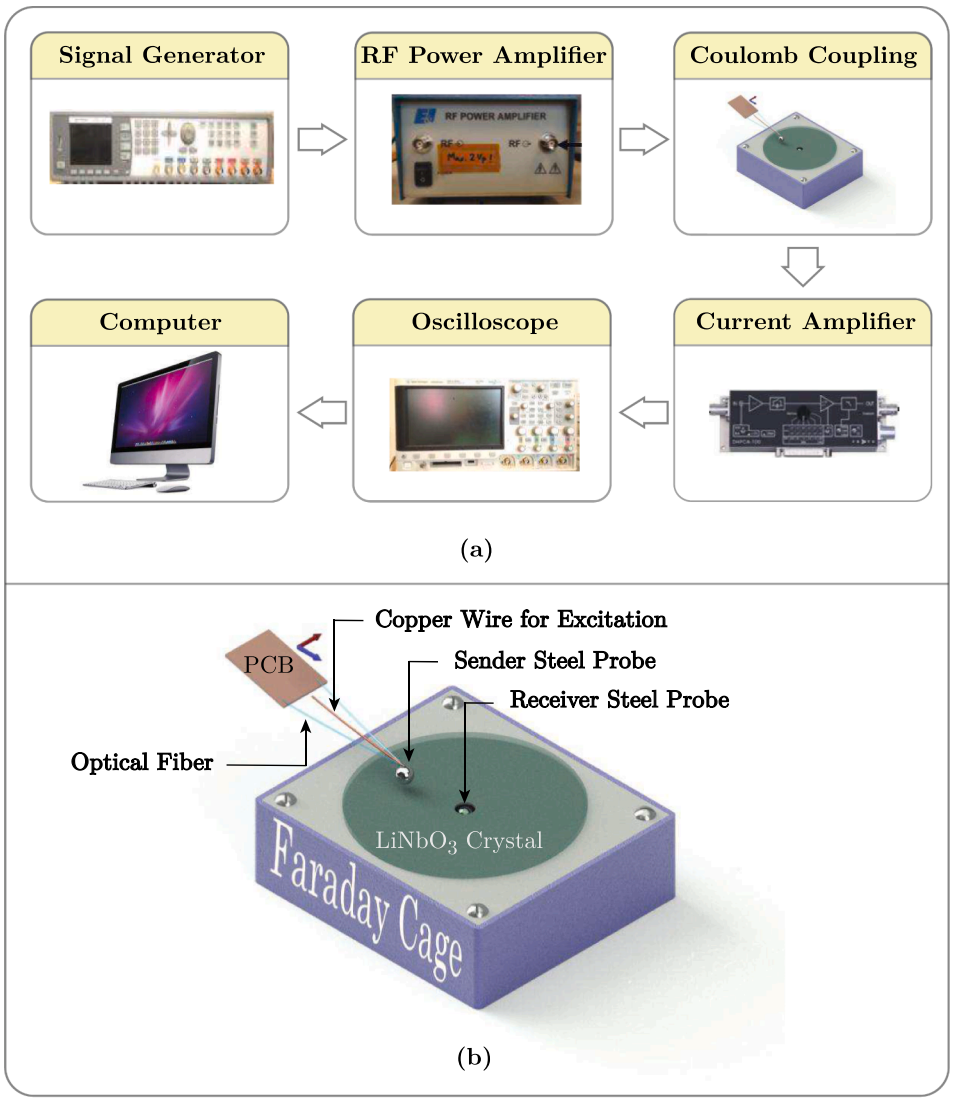

Fig. 3. a) Schematic diagram of the signal generation and detection through local electrical field probe, and b) detailed view of local electric field probe setup.

the sample surface. The motors were controlled by a computer via a serial interface. For the fabrication of the Coulomb probe, two small pieces of optical fibre were glued together with epoxy to form an angle of approximately 60 degrees. A steel sphere of 1.57 mm diameter was attached and used for the excitation point source at the contact point. The other ends of the glass fibres were glued to an Aluminium holder and were mounted on the XY translation stages. The steel probe converts electromagnetic waves into mechanical waves through the piezoelectric coupling property of the anisotropic crystal. The scanner moved the probe across the sample surface while the transient signal was registered and averaged at every position. In the current experimental setup, the detector was stationary and positioned at the centre, whereas the excitation probe emitted acoustic waves at each pixel point.

The typical scan area was 20 mm $\times$ 20 mm, which was centred relative to the detector tip below the sample. The acoustic wave was excited using a short pulse of 35 ns duration in $LiNbO_3$ (X-cut, 1 mm thick, both sides optically polished) crystal. During the time synchronized scan, the received signal was acquired from the opposite side of the $LiNbO_3$ crystal with a similar local electric field probe. Later on, the received signal was then amplified using a *trans*-impedance amplifier which converts the current into voltage according to an amplifying factor. The amplified signal is then acquired by an oscilloscope which averages and digitizes the signal. The digitized signal is then recorded using a personal computer. Two-dimensional spatiotemporal imaging of acoustic wave propagation was rendered using the time-resolved voltage data at each pixel point.

4. Theory

4.1. Christoffel equation

The stiffness tensor $\boldsymbol{C}$ is an elementary characteristic of a material. It relates stresses and strains within the elastic limit by generalizing the three-dimensional Hooke's law.

$$T_{ij} = \sum_{mn} C_{ijmn} S_{mn} \tag{9}$$

where, T is the stress tensor and S is the strain tensor. The generalized stiffness matrix $\boldsymbol{C}$ is a second-order tensor, and for non-polar material, it is expressed by 6×6 matrix.

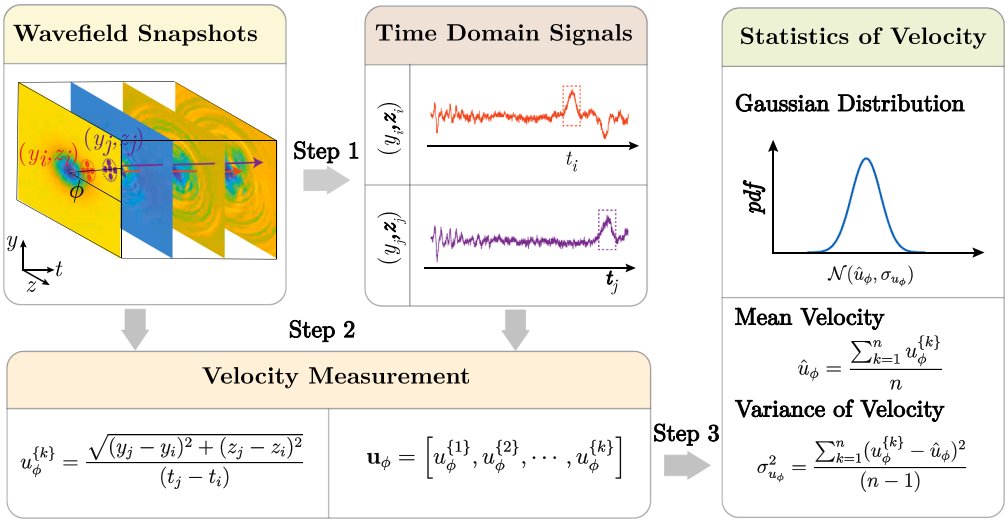

Fig. 4. Illustration of the steps involved in the computation of the statistical velocity.

$$\boldsymbol{C} = \begin{bmatrix} C_{11} & C_{12} & C_{13} & C_{14} & C_{15} & C_{16} \\ C_{21} & C_{22} & C_{23} & C_{24} & C_{25} & C_{26} \\ C_{31} & C_{32} & C_{33} & C_{34} & C_{35} & C_{36} \\ C_{41} & C_{42} & C_{43} & C_{44} & C_{45} & C_{46} \\ C_{51} & C_{52} & C_{53} & C_{54} & C_{55} & C_{56} \\ C_{61} & C_{62} & C_{63} & C_{64} & C_{65} & C_{66} \end{bmatrix} \tag{10}$$

In addition to the information about static deformations, the propagation of the elastic wave in a material is governed by the structural form of the stiffness tensor. The evolution and propagation of the longitudinal and transversal bulk wave in an anisotropic crystal are illustrated with the Christoffel equation [54].

$$\left[\Gamma_{ij} - \rho\omega^2\delta_{ij}\right]U_j = 0 \tag{11}$$

For a monochromatic wave with frequencyω, polarisation $\overrightarrow{U}$ and wave vector $\boldsymbol{n}$ propagating through a material of densityρ, then the Christoffel matrix Γ is defined as:

$$\Gamma_{ij} = n_m C_{imnj} n_j \tag{12}$$

The Eq. (11) is a simple Eigenvalue problem that can be solved systematically for any value of$\boldsymbol{n}$. The Eigenvalue solution consists of three frequencies that ultimately lead to the three-phase velocities for each value of$\boldsymbol{n}$. For $LiNbO_3$, which is a trigonal crystal, in the *YZ* plane polarisation along the *X-axis,* the velocity of the pure shear wave, $u^{(2)}$ along the propagation angle ϕ is given by [32]

$$u^{(2)} = \frac{1}{\rho^{1/2}\left\{C_{66}\sin^2\phi + C_{44}\cos^2\phi + C_{14}\sin 2\phi\right\}^{1/2}} \tag{13}$$

The velocity of the Quasi-shear wave, $u^{(1)}$ is described by

$$u^{(1)} = \frac{1}{(2\rho)^{1/2}\left\{P - \sqrt{Q^2 + R}\right\}^{-1/2}} \tag{14}$$

The velocity of the Quasi-longitudinal, $u^{(3)}$ wave is described by

$$u^{(3)} = \frac{1}{(2\rho)^{1/2}\left\{P + \sqrt{Q^2 + R}\right\}^{-1/2}} \tag{15}$$

where,

$$\begin{aligned} P &= C_{44} + C_{11}\sin^2\phi + C_{33}\cos^2\phi - C_{14}\sin 2\phi \\ Q &= (C_{44} - C_{11})\sin^2\phi + (C_{33} - C_{44})\cos^2\phi + C_{14}\sin 2\phi \\ R &= \left\{(C_{13} + C_{14})\sin 2\phi - 2C_{14}\sin^2\phi\right\}^2 \end{aligned} \tag{16}$$

4.2. Calculation of wave velocity

Considering an arbitrary Cartesian coordinate system in the plane of an anisotropic substrate, a particular wave mode travelled at time t_i from a location $\left(y_i, z_i\right)$, and it reached the location $\left(y_j, z_j\right)$ at timet_j. The velocity of a wave along an angle ϕ can be computed as:

$$u_\phi^{\{k\}} = \frac{\sqrt{\left(y_j - y_i\right)^2 + \left(z_j - z_i\right)^2}}{\left(t_j - t_i\right)} \tag{17}$$

The velocity is computed repeatedly in several adjacent points along a particular radial direction $(k = 1, 2, \cdots, n)$ to evaluate the uncertainty in the velocity measurement. For anisotropic material, the wave velocity depends on the direction of propagation ϕ and can be defined as:

$$\phi = \tan^{-1}\left(\frac{z_j - z_i}{y_j - y_i}\right) \tag{18}$$

$$\boldsymbol{u}_\phi = \left[u_\phi^{\{1\}}, u_\phi^{\{2\}}, \cdots, u_\phi^{\{n\}}\right] \tag{19}$$

where, $\boldsymbol{u}_\phi$ is a vector representing a collection of all the velocities calculated at various points along the propagationϕ. An illustration of the steps involved in the computation of the velocity and the corresponding uncertainty is presented in Fig. 4. It is assumed that the probability distribution function of the velocity follows the Gaussian distribution. The sample mean, $\widehat{u}_\phi$ and sample variance, $\sigma^2_{u_\phi}$ can be computed as follows:

$$\widehat{u}_\phi = \frac{\sum_{k=1}^{n} u_\phi^{\{k\}}}{n} \tag{20}$$

$$\sigma^2_{u_\phi} = \frac{\sum_{k=1}^{n}\left(u_\phi^{\{k\}} - \widehat{u}_\phi\right)^2}{(n-1)} \tag{21}$$

5. Unscented Kalman filter

One of the key components in the development of the proposed framework is to estimate the constitutive parameters from the velocity

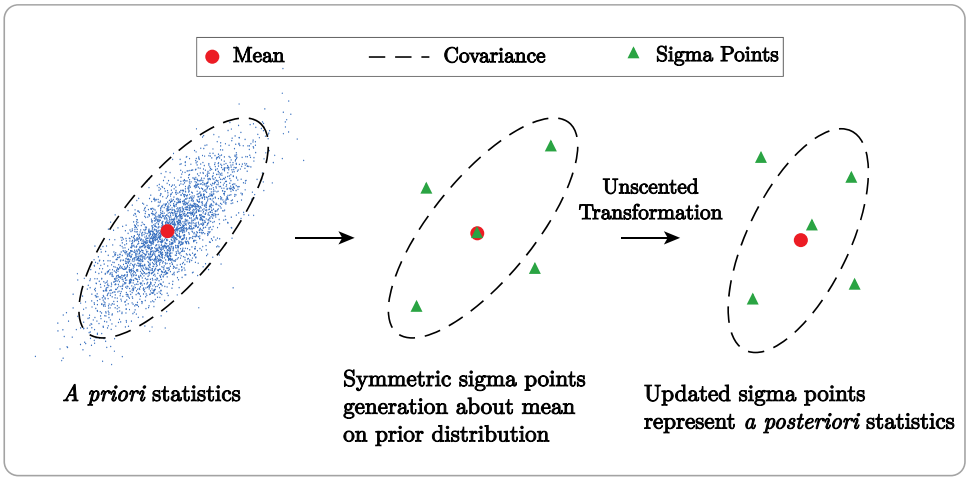

Fig. 5. Illustration of unscented transformation of a distribution using sigma points.

profile. This is can be considered as a classical parameter estimation problem, and this study proposes to employ the Bayesian filter to achieve the objective. Bayesian filters utilise Bayesian inference to formulate a framework that can be used for parameter estimation. Bayesian inference differs from the conventional frequentist approach (e.g., maximum likelihood estimation (MLE)). The Bayesian inference takes the uncertainty of an event in a single trial as the probability of an event. In contrast, the frequentist approach considers it as the proportion of the event in probability space, despite the fact that the full posterior estimation in the Bayesian approach is accurate but computationally expensive and is often intractable. The first-order Markovian process assumption simplifies the computational intricacy. Using assumptions of the Markovian model, the recursive Bayesian filter can be established, and the Kalman filter emerges [55,56]. The Kalman filter is a particular type of recursive Bayesian filter applied for a linear model. The extended Kalman filter (EKF) [55] and unscented Kalman filter (UKF) [55,57] are advancements over the Kalman filter to apply for non-linear models. In this study, UKF is used as a Bayesian filter of choice over the other Bayesian filter and the conventional frequentist approach. It is to be noted that the UKF is computationally expensive as compared to the EKF and MLE; however, the performance of the UKF in the case of non-linear systems and small observed data regime is superior [57]. Indeed, powered by the increased computational resources, the proposed UKF based framework results as robust and reliable for the parameter estimation task.

The solution of the Christoffel equation prescribes a set of mathematical models of the velocity of a wave in a material. For instance, the governing equation describes the velocity of the Quasi-shear wave in Lithium Niobate crystal in the *YZ* plane given in the Eq. (14) is a complex non-linear system. The unscented Kalman filter (UKF) is a versatile filter appropriate for complex non-linear systems first developed by Julier and Uhlman [58]. It utilizes the concept of unscented transformation to approximate the statistics of fairly complex non-linear systems. In the unscented transformation, the statistical properties of a random variable are approximated by choosing a set of sample points deterministically. These points are known as sigma points. Each sigma point is propagated through the non-linear systems to apply the non-linear transformation. These transformed sets of points represent the statistical properties of the transformed random variable. Fig. 5 illustrates how sigma points are employed in the unscented transformation to represent *a posteriori* statistic.

Let us consider a general discrete non-linear dynamic system modelled as

$$\begin{aligned} \boldsymbol{x}_{k+1} &= \boldsymbol{F}(\boldsymbol{x}_k) + \boldsymbol{w}_k \\ \boldsymbol{y}_k &= \boldsymbol{H}(\boldsymbol{x}_k) + \boldsymbol{v}_k \end{aligned} \tag{22}$$

where, $\boldsymbol{F} : \mathbb{R}^N \mapsto \mathbb{R}^N$ is the vector-valued state prediction function of the system, $\boldsymbol{H} : \mathbb{R}^N \mapsto \mathbb{R}^M$ is the observation function that transforms a state vector into the proper measurement vector. The $\boldsymbol{x}_k \in \mathbb{R}^N$ is the state variable, $\boldsymbol{y}_k \in \mathbb{R}^M$ is the measured value, and $\boldsymbol{w}_k \in \mathbb{R}^N$ and $\boldsymbol{v}_k \in \mathbb{R}^M$ are additive process noise with covariance $\boldsymbol{Q}$ and measurement noise with covariance$\boldsymbol{R}$, respectively, as in the Eq. (23). The subscript $k \in \mathbb{N}$ denotes the k - th discrete step.

$$\begin{aligned} \boldsymbol{w}_k &\sim \mathcal{N}(\boldsymbol{0}, \mathbf{Q}_k) \\ \boldsymbol{v}_k &\sim \mathcal{N}(\boldsymbol{0}, \mathbf{R}_k) \\ E\left[\boldsymbol{w}_k \boldsymbol{v}_k^T\right] &= \boldsymbol{0} \end{aligned} \tag{23}$$

It is assumed that the state variable $\boldsymbol{x}_k \in \mathbb{R}^N$ obeys a normal distribution with its mean $\widehat{\boldsymbol{x}}_k$ and covariance $\boldsymbol{P}_k$ denoted by$\boldsymbol{x}_k \sim \mathcal{N}(\widehat{\mathbf{x}}_k, \mathbf{P}_k)$. We also suppose that the initial state,$\widehat{\boldsymbol{x}}_0$, is known with the corresponding initial error covariance matrix,$\boldsymbol{P}_0$. The UKF algorithm is discussed briefly in the following section 5.1. A probabilistic approach to the key steps involved within the UKF framework is shown

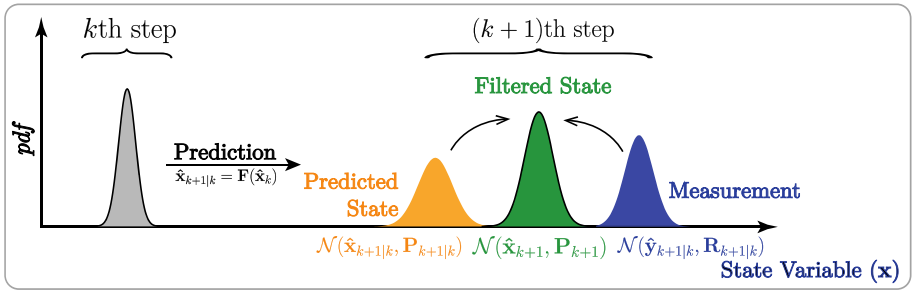

Fig. 6. Schematic presentation of the steps involved in the unscented Kalman filter algorithm.

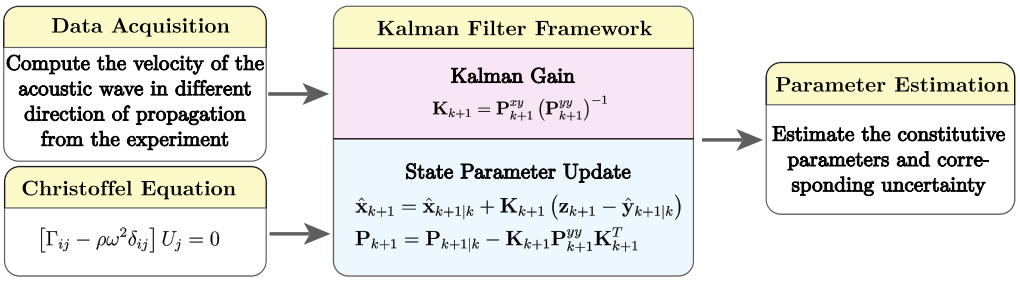

Fig. 7. Flowchart representing key components of the proposed parameter estimation algorithm.

schematically in Fig. 6.

5.1. Unscented Kalman filter (UKF) algorithm

Step 1: Calculation of weights for sigma points

A set of weights $\boldsymbol{W}^{(i)}$ corresponding to each sigma point are defined as follows:

$$\begin{aligned} \boldsymbol{W}^{(0)} &= \frac{\kappa}{N+\kappa} \\ \boldsymbol{W}^{(i)} &= \frac{1}{2(N+\kappa)}, \; i = 1, 2, ..., 2N \end{aligned} \tag{24}$$

where, the parameter κ is the scaling parameter that controls the spread of the sigma point about the mean, $\widehat{\boldsymbol{x}}_{k|k}$ and N is the length of the state vector. κ can take any positive or negative value such that$N + \kappa \neq 0$. In this study, it has been chosen$\kappa = 0$.

Step 2: Define noise

Define process and measurement noise covariance matrices as:

$$\begin{aligned} \boldsymbol{Q}_k &= E\left[\boldsymbol{w}_k \boldsymbol{w}_k^T\right] \\ \boldsymbol{R}_k &= E\left[\boldsymbol{v}_k \boldsymbol{v}_k^T\right] \end{aligned} \tag{25}$$

Step 3: Initialization

Define the initial state vector and corresponding error covariance matrix as:

$$\begin{aligned} \widehat{\boldsymbol{x}}_0 &= E[\boldsymbol{x}_0] \\ \boldsymbol{P}_0 &= E\left[(\boldsymbol{x}_0 - \widehat{\boldsymbol{x}}_0)(\boldsymbol{x}_0 - \widehat{\boldsymbol{x}}_0)^T\right] \end{aligned} \tag{26}$$

Step 4: Generate the sigma points

A set of $2N+1$ sigma points $\boldsymbol{\chi}_k^{(i)}$ are defined as follows:

$$\begin{aligned} \boldsymbol{\chi}_k^{(0)} &= \widehat{\boldsymbol{x}}_k, \\ \boldsymbol{\chi}_k^{(i)} &= \widehat{\boldsymbol{x}}_k + \sqrt{N+\kappa}\left(\sqrt{\boldsymbol{P}_k}\right)_i, \\ \boldsymbol{\chi}_k^{(i+N)} &= \widehat{\boldsymbol{x}}_k - \sqrt{N+\kappa}\left(\sqrt{\boldsymbol{P}_k}\right)_i \end{aligned} \tag{27}$$

where $\left(\sqrt{\boldsymbol{P}_k}\right)_i$ is the i - th column of the matrix square root of the error covariance matrix$\boldsymbol{P}_k$. The weighted covariance matrix of $\boldsymbol{\chi}$ is $\boldsymbol{P}_k$ can be computed as:

$$\boldsymbol{P}_k = \sum_{i=0}^{2N} \boldsymbol{W}_k^{(i)} \left(\boldsymbol{\chi}_k^{(i)} - \widehat{\boldsymbol{x}}_k\right)\left(\boldsymbol{\chi}_k^{(i)} - \widehat{\boldsymbol{x}}_k\right)^T \tag{28}$$

Step 5: Prediction

Propagate each sigma points through the prediction model

$$\boldsymbol{\chi}_{k+1|k}^{(i)} = \boldsymbol{F}\left(\boldsymbol{\chi}_k^{(i)}\right), \; i = 0, 1, ..., 2N \tag{29}$$

Calculate the mean $\widehat{\boldsymbol{x}}_{k+1|k}$ and covariance $\boldsymbol{P}_{k+1|k}$ of the predicted state as given by:

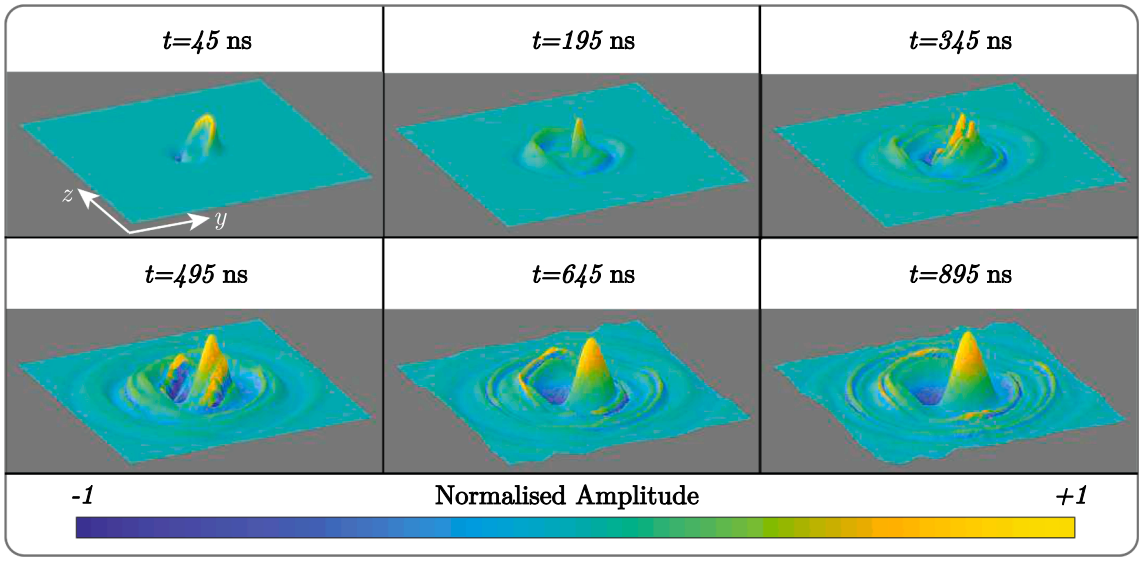

Fig. 8. Pseudo-3D representation of the ultrasonic wave propagation on X-cut 300 μm thick $LiNbO_3$ crystal obtained for the finite element method simulation case. Each frame dimension is 8 mm × 8 mm.

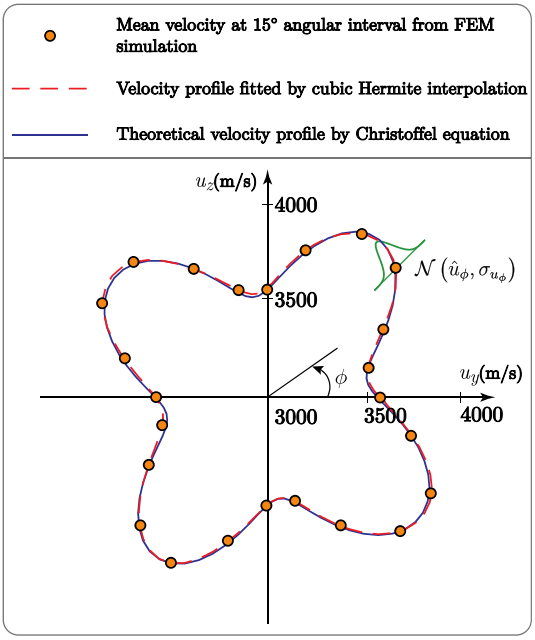

Fig. 9. The ultrasonic velocity profile computed from finite element method simulation in various directions for Lithium Niobate crystal.

$$\hat{\boldsymbol{x}}_{k+1|k} = \sum_{i=0}^{2N} \boldsymbol{W}^{(i)} \boldsymbol{\chi}_{k+1|k}^{(i)}$$
$$\boldsymbol{P}_{k+1|k} = \sum_{i=0}^{2N} \boldsymbol{W}^{(i)} \left(\boldsymbol{\chi}_{k+1|k}^{(i)} - \hat{\boldsymbol{x}}_{k+1|k}\right)\left(\boldsymbol{\chi}_{k+1|k}^{(i)} - \hat{\boldsymbol{x}}_{k+1|k}\right)^T + \boldsymbol{Q}_{k+1} \tag{30}$$

Step 6: Observation

Propagate each sigma point through observation

$$\boldsymbol{\psi}_{k+1|k}^{(i)} = \boldsymbol{H}\left(\boldsymbol{\chi}_{k+1|k}^{(i)}\right), \; i = 0, 1, ..., 2N \tag{31}$$

Calculate the mean$\hat{\boldsymbol{y}}_{k+1|k}$, covariance of predicted output$\boldsymbol{P}_{k+1}^{yy}$, and cross-covariance of state and output $\boldsymbol{P}_{k+1}^{xy}$ as given by:

$$\hat{\boldsymbol{y}}_{k+1|k} = \sum_{i=0}^{2N} \boldsymbol{W}^{(i)} \boldsymbol{\psi}_{k+1|k}^{(i)},$$
$$\boldsymbol{P}_{k+1}^{yy} = \sum_{i=0}^{2N} \boldsymbol{W}^{(i)} \left(\boldsymbol{\psi}_{k+1|k}^{(i)} - \hat{\boldsymbol{y}}_{k+1|k}\right)\left(\boldsymbol{\psi}_{k+1|k}^{(i)} - \hat{\boldsymbol{y}}_{k+1|k}\right)^T + \boldsymbol{R}_{k+1} \tag{32}$$
$$\boldsymbol{P}_{k+1}^{xy} = \sum_{i=0}^{2N} \boldsymbol{W}^{(i)} \left(\boldsymbol{\chi}_{k+1|k}^{(i)} - \hat{\boldsymbol{x}}_{k+1|k}\right)\left(\boldsymbol{\psi}_{k+1|k}^{(i)} - \hat{\boldsymbol{y}}_{k+1|k}\right)^T$$

Step 7: Update

Compute Kalman gain$\boldsymbol{K}_k$, filtered state mean $\hat{\boldsymbol{x}}_{k+1}$ and error covariance $\boldsymbol{P}_{k+1}$ provided the sensor measurement z_{k+1} as follows:

$$\boldsymbol{K}_{k+1} = \boldsymbol{P}_{k+1}^{xy} \left(\boldsymbol{P}_{k+1}^{yy}\right)^{-1}$$
$$\hat{\boldsymbol{x}}_{k+1} = \hat{\boldsymbol{x}}_{k+1|k} + \boldsymbol{K}_{k+1}\left(z_{k+1} - \hat{\boldsymbol{y}}_{k+1|k}\right) \tag{33}$$
$$\boldsymbol{P}_{k+1} = \boldsymbol{P}_{k+1|k} - \boldsymbol{K}_{k+1} \boldsymbol{P}_{k+1}^{yy} \boldsymbol{K}_{k+1}^T$$

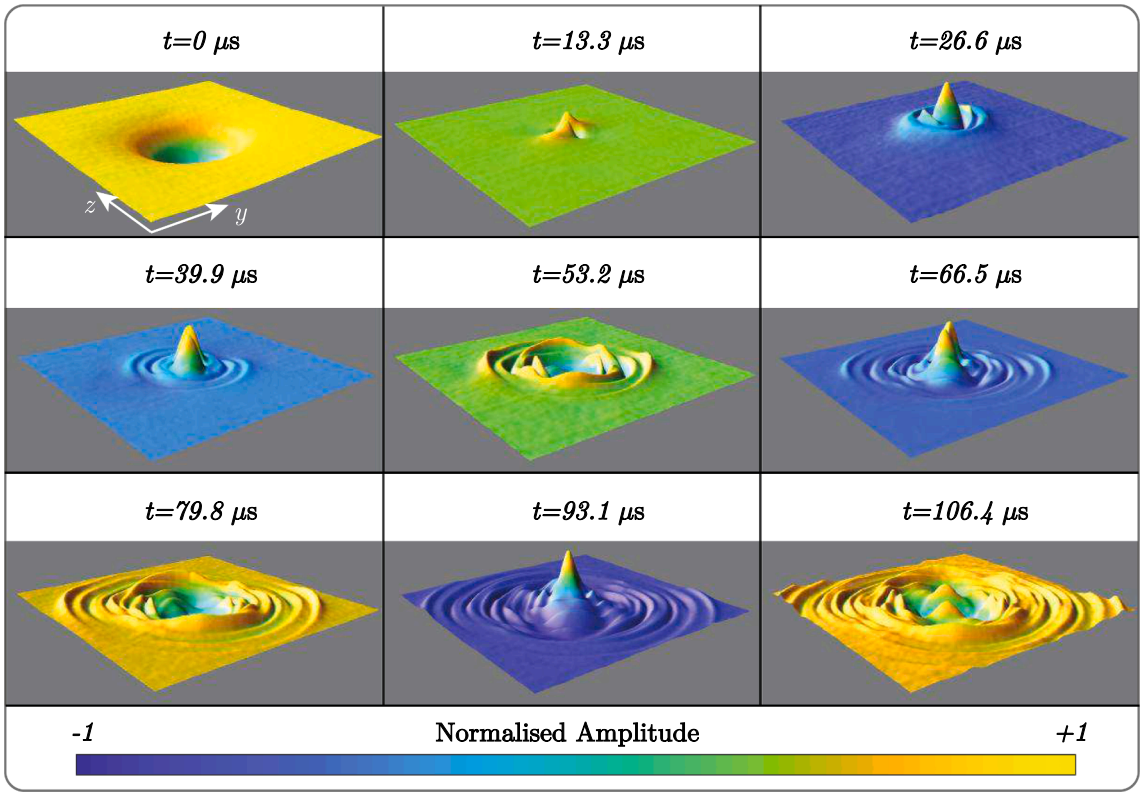

Fig. 10. Pseudo-3D representation of the spatial and temporal evolution of the ultrasonic wave amplitude of images on X orientation 1 mm thick, $LiNbO_3$ crystal at a gate width of 35 ns for the experimental case. Each image frame dimension is 20 mm × 20 mm.

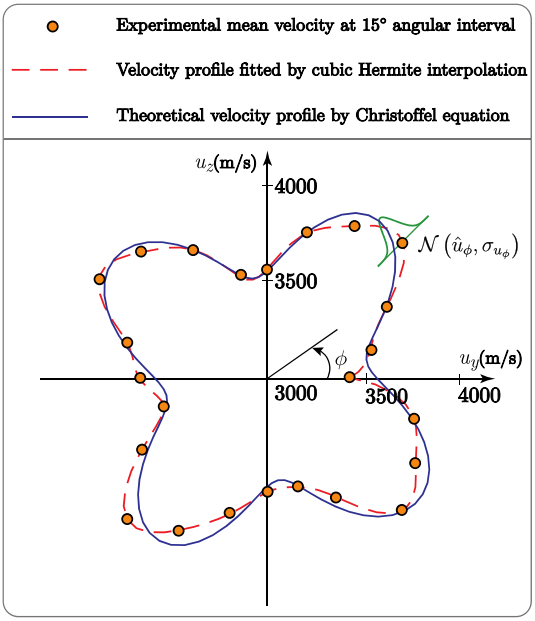

Fig. 11. The variation of ultrasonic velocity in different directions evaluated from the experiment for Lithium Niobate crystal.

The UKF is used for the estimation of constitutive parameters of an anisotropic crystal. The essential parts of the robust inversion algorithm are illustrated in Fig. 7.

6. Results and discussions

6.1. FEM simulation results

The transient time domain signals obtained at various points from the simulation are used to visualise the ultrasonic wave in the $LiNbO_3$ crystal. Fig. 8 shows the visualisation of wave propagation in the $LiNbO_3$ crystal acquired through FEM simulation. The total acquisition time of the temporal images of 1 μs corresponding to 201 time-varying snapshots. Each frame of Fig. 8 corresponds to 150 ns in the transient signals. The numerical velocity results are incorporated in the UKF algorithm for establishing the accuracy of the parameter estimation.

The Kalman filter utilized the combined information of field measurement and governing mechanistic equation for the estimation of state parameters. However, to illustrate the efficiency of the Kalman filter algorithm, we measured the velocity at an angular spacing of 15° varying from 0° to360°.

In Fig. 9, the blue line represents the theoretical velocity profile for the Quasi-shear wave in $LiNbO_3$ crystal, which is computed by the Eigen solution of the Christoffel equation. Further, the circle legends represent the numerical average velocity of the ultrasonic wave calculated along a particular direction of propagation. Upon computing discrete velocity in different directions, a cubic Hermite interpolation was performed to approximate the velocity in all directions. The resulting profile is shown by the red dashed line in Fig. 9. However, this approximate velocity profile does not require in the UKF framework.

6.2. Experimental results

We present the visualization of propagation of the ultrasonic wave in $LiNbO_3$ acquired through the Coulomb Coupling method. After the acquisition of the transient signals for every position of the scanner, time gating was performed to construct the snapshot of the ultrasound waves.

Fig. 10 shows the pseudo-3D evolution of ultrasonic waves in $LiNbO_3$ crystal at an excitation gate width of 35 ns. The speed of the ultrasonic wave in an anisotropic solid is directional dependent and evident from Fig. 10. Each frame of Fig. 10 corresponds to 13.3 µs in the transient signal. The brightness of the images indicates wavefront on the crystal surface at the corresponding gating time. The velocity of the ultrasonic wave in each direction is calculated from the evolution of spatiotemporal snapshots. The advantage of the Coulomb coupling technique is it provides complete field transient imaging, so it is possible to compute the velocity in every direction.

The theoretical velocity profile computed by the Eigen solution of the Christoffel equation for the Quasi-shear wave in $LiNbO_3$ crystal is presented by the blue line in Fig. 11. The circle legends in Fig. 11 illustrate the average experimental velocities calculated in a particular direction of propagation. The dashed red line in Fig. 11 shows the interpolated velocity profile.

6.3. Vefification of UKF algorithm using FEM simulation data

The transient time domain signals obtained at various points from the simulation are used to visualise the ultrasonic wave in the $LiNbO_3$ crystal, as shown in Fig. 8. The velocity of the propagated wave along different directions is computed from the simulation data. The constitutive parameters estimation of the crystal from the velocity data is an ill-posed inverse problem, and the noisy/uncertain velocity data compounds this challenge.

Usually, the data obtained from the simulation are more accurate and noise-free compared to the data collected from real field experiments. Moreover, in the case of simulation, the parameters to be estimated are known *a priori*. In general, starting with a problem where the solution is known is important to evaluate the performance and verify the architecture of the proposed algorithm. Thus, we evaluate the performance of the algorithm by comparing the estimated parameters with the known parameters (theoretical value) used in the FEM simulation.

To illustrate the performance of the UKF in parameter estimation, we considered the non-linear characteristic model for Quasi-shear wave propagation as expressed in the Eq. (14). We considered that the velocity measurements are available in different directions. The objective here is to estimate the constitutive parameters accurately by diffusing the mathematical model and the experimental measurements available in the UKF framework. Fig. 9 shows the variation of mean velocity, $\widehat{u}$ with respect to the angle ϕ extracted from the FEM simulation.

For the parameter estimation using UKF, an augmented state vector $\boldsymbol{x}$ is defined as:

$$\boldsymbol{x} = \begin{bmatrix} x_1 \\ x_2 \\ x_3 \\ x_4 \\ x_5 \end{bmatrix} = \begin{bmatrix} C_{11} \\ C_{13} \\ C_{14} \\ C_{33} \\ C_{44} \end{bmatrix} \tag{34}$$

Then the state space is formulated as follows:

$$\dot{\boldsymbol{x}} = \begin{bmatrix} \dot{x}_1 \\ \dot{x}_2 \\ \dot{x}_3 \\ \dot{x}_4 \\ \dot{x}_5 \end{bmatrix} = \begin{bmatrix} 0 \\ 0 \\ 0 \\ 0 \\ 0 \end{bmatrix} \tag{35}$$

The derivatives with respect to the time of the constitutive parameters are all zero because they are assumed to be constant over time. A discrete form of the Eq. (35) is given by:

Table 2
Sigma points of the initial state vector in unscented Kalman filter framework for the finite element method simulation case.

Sigma Point	1	2	3	4	5	6	7	8	9	10	11
$C_{11}\left(\times 10^{10}\ \mathrm{N/m^2}\right)$	10	12.815	10	10	10	10	7.185	10	10	10	10
$C_{13}\left(\times 10^{10}\ \mathrm{N/m^2}\right)$	0.2	0.2	3.015	0.2	0.2	0.2	0.2	−2.615	0.2	0.2	0.2
$C_{14}\left(\times 10^{10}\ \mathrm{N/m^2}\right)$	0.3	0.3	0.3	0.524	0.3	0.3	0.3	0.3	0.076	0.3	0.3
$C_{33}\left(\times 10^{10}\ \mathrm{N/m^2}\right)$	12	12	12	12	14.815	12	12	12	12	9.185	12
$C_{44}\left(\times 10^{10}\ \mathrm{N/m^2}\right)$	3	3	3	3	3	5.815	5	5	5	5	0.185

$$\boldsymbol{x}_{k+1} = \boldsymbol{F}(\boldsymbol{x}_k) + \boldsymbol{w}_k = \begin{bmatrix} x_{1,k} \\ x_{2,k} \\ x_{3,k} \\ x_{4,k} \\ x_{5,k} \end{bmatrix} + \boldsymbol{w}_k \tag{36}$$

where a process noise $\boldsymbol{w}$ has been added.

If the velocity of the wave propagation in a crystal is measured, the observation equation can be expressed as:

$$y = u + v \tag{37}$$

where u is the velocity of the wave and v represents the measurement noise.

The vector-valued non-linear function $\boldsymbol{H}$ in Eq. (22) can be defined by Eq. (14) written as follows:

$$\boldsymbol{y}_k = \boldsymbol{H}(\boldsymbol{x}_k) + \boldsymbol{v}_k = \frac{1}{(2\rho)^{1/2}\left\{P - \sqrt{Q^2 + R}\right\}^{-1/2}} + v_k \tag{38}$$

By combining the Eqs. (16) and (34), the P, Q and R of the Eq. (38) are re-written as follows:

$$\begin{aligned} P &= x_{5,k} + x_{1,k}\sin^2\phi + x_{4,k}\cos^2\phi - x_{3,k}\sin 2\phi \\ Q &= \left(x_{5,k} - x_{1,k}\right)\sin^2\phi + \left(x_{4,k} - x_{5,k}\right)\cos^2\phi + x_{3,k}\sin 2\phi \\ R &= \left\{\left(x_{2,k} + x_{3,k}\right)\sin 2\phi - 2x_{3,k}\sin^2\phi\right\}^2 \end{aligned} \tag{39}$$

To perform the parameter estimation using the UKF, the iteration process initiates within the UKF framework by initializing the state vector estimate $\hat{\boldsymbol{x}}_0$ and its error covariance matrix$\boldsymbol{P}_0$. It was observed that naively applying UKF to data with uncertainty for parameter estimation would often result in incorrect estimation, as the effects of noise variance in the data set. Hence, we configure the initial state vector estimate $\hat{\boldsymbol{x}}_0$ and the initial covariance matrix $\boldsymbol{P}_0$ to ensure that the UKF can be applied as follows:

$$\begin{aligned} \hat{\boldsymbol{x}}_0 &= \left[C_{11,0}, C_{13,0}, C_{14,0}, C_{33,0}, C_{44,0}\right]^T = \left[10\times 10^1, 0.2\times 10^1, 0.3\times 10^1, 12\times 10^1, 3\times 10^1\right]^T \mathrm{GPa} \\ \boldsymbol{P}_0 &= diag(\sigma^2_{C_{11,0}}, \sigma^2_{C_{13,0}}, \sigma^2_{C_{14,0}}, \sigma^2_{C_{33,0}}, \sigma^2_{C_{44,0}}) = diag(1.58\times 10^2, 1.58\times 10^2, 1, 1.58\times 10^2, 1.58\times 10^2)\ \mathrm{GPa}^2 \end{aligned} \tag{40}$$

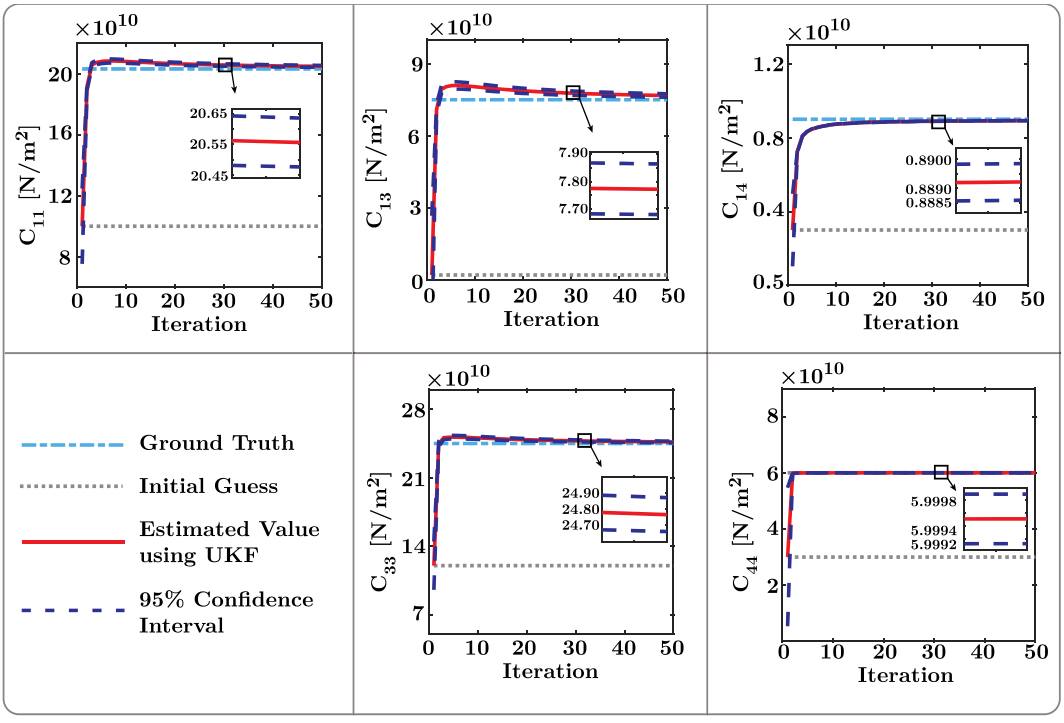

Fig. 12. Constitutive parameter estimation results for the Lithium Niobate crystal for finite element method simulation case. The velocity with uncertainty computed from the finite element method simulation is provided to the unscented Kalman filter as a measurement.

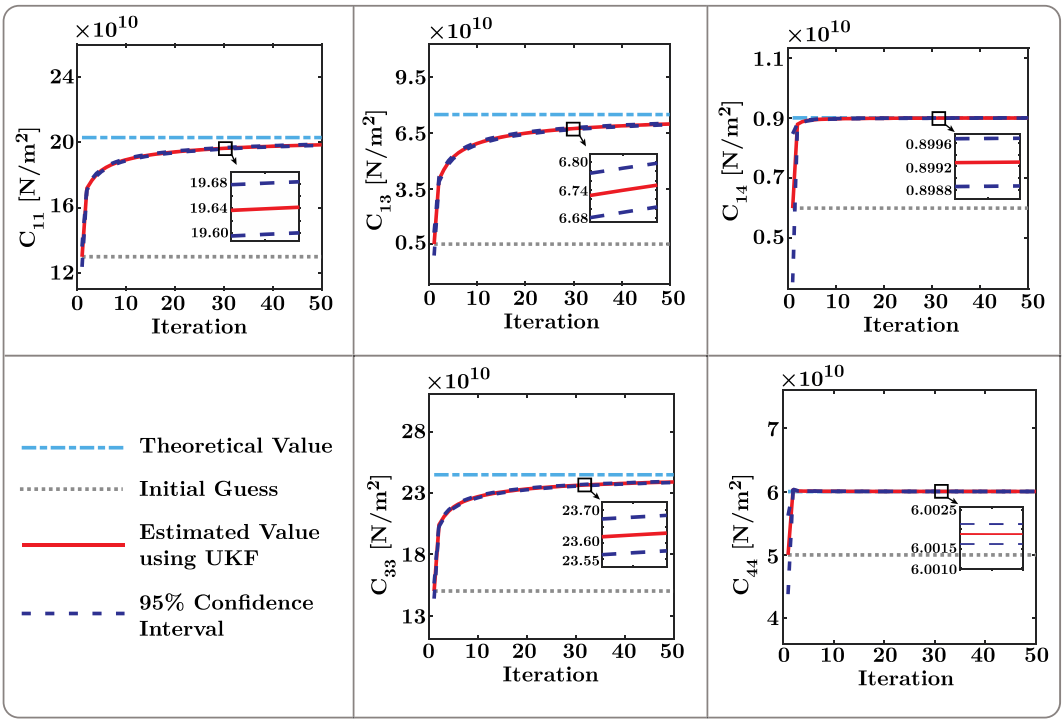

Fig. 13. Constitutive parameter estimation results for the Lithium Niobate crystal for the experimental case. The velocity measurement perturbated with uncertainty from the experiment is provided to the unscented Kalman filter as a measurement.

Table 3
Summary of the constitutive parameter estimation for the finite element method simulation case.

Constitutive Parameters	Theoretical Value	Initial Guess	Estimated	Relative % Error (±)
C_{11} ($\times 10^{10}$N/m^2)	20.3	10	20.47	0.84 %
C_{13} ($\times 10^{10}$N/m^2)	7.5	0.2	7.67	2.27 %
C_{14} ($\times 10^{10}$N/m^2)	0.9	0.3	0.89	1.11 %
C_{33} ($\times 10^{10}$N/m^2)	24.5	12	24.66	0.65 %
C_{44} ($\times 10^{10}$N/m^2)	6.0	3	5.99	0.20 %

Table 5
Summary of the constitutive parameter estimation for the experimental case.

Constitutive Parameters	Theoretical Value	Initial Guess	Estimated	Relative % Error (±)
C_{11} ($\times 10^{10}$N/m^2)	20.3	13	19.86	2.17 %
C_{13} ($\times 10^{10}$N/m^2)	7.5	0.5	6.99	6.80 %
C_{14} ($\times 10^{10}$N/m^2)	0.9	0.6	0.89	1.11 %
C_{33} ($\times 10^{10}$N/m^2)	24.5	15	23.91	2.41 %
C_{44} ($\times 10^{10}$N/m^2)	6.0	5	6.001	0.02 %

where $diag(\cdot)$ is a diagonal matrix with arguments along the main diagonal. Further, the process noise covariance matrix $\boldsymbol{Q}$ is set to be null, since the state $\boldsymbol{x}$ has no superimposed noise. The measurement noise is assumed to be a Gaussian white noise process with zero mean and covariance matrix $\boldsymbol{R}$ with the terms along the main diagonal are defined in the Eq. (21).

$$\boldsymbol{R} = \begin{bmatrix} \sigma^2_{u_{0^\circ}} & 0 & \cdots & 0 \\ 0 & \sigma^2_{u_{15^\circ}} & \circ & \vdots \\ \vdots & \circ & \ddots & 0 \\ 0 & \cdots & 0 & \sigma^2_{u_{360^\circ}} \end{bmatrix} \tag{41}$$

Table 4
Sigma points of the initial state vector in the unscented Kalman filter framework for the experimental case.

Sigma Point	1	2	3	4	5	6	7	8	9	10	11
$C_{11}\left(\times 10^{10}\ \mathrm{N/m^2}\right)$	13	13.707	13	13	13	13	12.293	13	13	13	13
$C_{13}\left(\times 10^{10}\ \mathrm{N/m^2}\right)$	0.5	0.5	1.207	0.5	0.5	0.5	0.5	−0.207	0.5	0.5	0.5
$C_{14}\left(\times 10^{10}\ \mathrm{N/m^2}\right)$	0.6	0.6	0.6	5.055	0.6	0.6	0.6	0.6	0.318	0.6	0.6
$C_{33}\left(\times 10^{10}\ \mathrm{N/m^2}\right)$	15	15	15	15	15.707	15	15	15	15	14.293	15
$C_{44}\left(\times 10^{10}\ \mathrm{N/m^2}\right)$	5	5	5	5	5	5.707	5	5	5	5	4.293

In the context of the general experimental procedure, it is assumed that the wave velocity measurements (z_k) in different directions are available by extracting data at every 15^0 angular spacing varying from 0^0 to 360^0.

$$z_k = \{\widehat{u}_{0^\circ}, \widehat{u}_{15^\circ}, \ldots, \widehat{u}_{360^\circ}\}^T \tag{42}$$

The UKF algorithm starts by generating eleven $(2N+1,$ here $N=5)$ sigma points deterministically based on $\widehat{\boldsymbol{x}}_0$ and $\boldsymbol{P}_0$ as defined in the Eq. (27). In the following step, each sigma point is employed to compute the wave velocity in the directions where field measurements are present. The algorithm will correct the initial guess in the first iteration by incorporating the innovations $\left(z_{k+1} - \widehat{y}_{k+1|k}\right)$ (difference between measurement and predicted measurement). This process continues recursively till the truncation criterion is achieved. The truncation criterion is achieved in this study by setting the minimum number of iterations to $50(k = 1,2,\ldots,50)$. However, one can achieve the truncation criterion by defining a tolerance limit ε as the absolute difference between the state vector estimates given by two successive Kalman Filter iterations(i.e. $\widehat{\boldsymbol{x}}_{k+1} - \widehat{\boldsymbol{x}}_k < \varepsilon$). The output of the UKF algorithm is the corrected state vector which is the mean $\widehat{\boldsymbol{x}}_k$ of the multivariate Gaussian distribution with the covariance matrix$\boldsymbol{P}_k$. Specifically, $\boldsymbol{P}_k$ stands for the uncertainty in estimating the constitutive parameters at k^{th} step.

For ease of reference, Table 2 and Table 4 present the generated sigma points, $\chi_0^{(i)}$ corresponding to the initial state vector within the UKF algorithm. Fig. 12 and Fig. 13 illustrate the parameter estimation results in terms of theoretical value and estimated parameters in every iteration. The dashed lines in Fig. 12 and Fig. 13 indicate the 95 % confidence interval (CI), implying the actual parameter lies between this interval with a probability of more than 0.95. The UKF being a Bayesian filter that has the capability to provide a level of confidence for the estimate, makes the algorithm superior to the other deterministic algorithms. We summarise the estimation of the constitutive parameter and corresponding absolute error in Table 3 and Table 5. It can be observed from Table 3 and Table 5 that the maximum error in the estimation of the stiffness parameters corresponds to the estimation ofC_{13}, that is less than 3 %.

6.4. Parameter estimation using UKF from experimental data

The performance and verification of the UKF algorithm are first examined and presented in section 6.3. To assess the performance of the proposed algorithm in the real experimental case, the mean velocity is computed from five samples along a particular direction of propagation. To that end, the velocity vector with uncertainty shown by circles in Fig. 11 is provided as the measurement in the UKF framework. For ease of reference, Table 4 shows the generated sigma points, $\chi_0^{(i)}$ corresponding to the initial state vector within the UKF algorithm for the experimental case.

The initial state vector estimate $\widehat{\boldsymbol{x}}_0$ and the initial covariance matrix $\boldsymbol{P}_0$ is configured to estimate the parameters within the UKF framework for the experimental case as follows:

$$\begin{aligned}\widehat{\boldsymbol{x}}_0 &= \left[C_{11,0}, C_{13,0}, C_{14,0}, C_{33,0}, C_{44,0}\right]^T = \left[13\times10^1, 0.5\times10^1, 0.6\times10^1, 15\times10^1, 5\times10^1\right]^T \text{GPa} \\ \boldsymbol{P}_0 &= diag(\sigma^2_{C_{11,0}}, \sigma^2_{C_{13,0}}, \sigma^2_{C_{14,0}}, \sigma^2_{C_{33,0}}, \sigma^2_{C_{44,0}}) = diag(10^1, 10^1, 0.158\times10^1, 10^1, 10^1)\ \text{GPa}^2\end{aligned} \tag{43}$$

where $diag(\cdot)$ is a diagonal matrix with arguments along the main diagonal.

The state parameter estimation results obtained by the proposed UKF algorithm are shown in Fig. 13. Fig. 13 illustrates the parameter estimation results in terms of theoretical value and estimated parameters in every iteration. The dashed lines in Fig. 13 indicate the 95 % confidence interval. It can be observed that the UKF algorithm provides remarkably accurate estimates of the constitutive parameters. As for the parameter estimation, C_{11}, C_{14}, C_{33} and C_{44} converge more accurately to the corresponding theoretical values, as given in Table 1. As forC_{13}, the proposed method acquires an accuracy of around 93 %. The estimation of the constitutive parameter and corresponding absolute error is summarised in Table 5.

From Table 3 and Table 5, two important observations can be drawn: (1) the error in the estimation of C_{44} is least as compared to the other parameters for both FEM and experimental cases. The least error in C_{44} is due to its sensitivity to the shape of the measured velocity profile and C_{44} is more sensitive; in other words, a slight change in the value of C_{44} there is a significant change in the velocity profile shape. Further, the rapidity of convergence and the error in the estimate of each parameter depends upon their sensitivity to the measurement provided in the UKF framework. The parameter C_{44} performs well in the estimation and has the minimum error; on the contrary, the constitutive parameter C_{13} has the maximum error as compared to the rest of the parameters for both FEM and experimental cases. However, the performance can further be improved by increasing the measurement size, i.e., a better representation of the velocity profile and by increasing the number of Kalman filter iterations. The aim of this work is to estimate the parameters optimally in the sparse measurement situation. (2) Some parameters, for instance, C_{11} andC_{13}, are over-estimated for the FEM simulation case but under-estimated in the experimental case. The under- and over-estimation of these parameters for both cases do not have any physical sense. Since the measured velocity profile and the amount of noise/uncertainty present in the measurement for FEM and experimental cases are different. Hence, each parameter does not need to follow a similar trend to converge its theoretical value in both cases. However, it is worth noting that the estimation error for each parameter should lie within the acceptable limit. From Table 3 and Table 5, one can observe that the parameters converge satisfactorily and the error corresponding to each estimation lies within the allowable limit.

7. Conclusion

The estimation of the mechanical properties of the anisotropic Lithium Niobate ($LiNbO_3$) is conducted using the Coulomb Coupling technique and Bayesian filtering. The point contact method based on Coulomb coupling is employed for the excitation and detection of ultrasonic waves in the $LiNbO_3$ crystal. The spatial–temporal wavefield imaging is utilized for the extraction of direction-dependent wave velocity. The direction wave velocity is a function of the stiffness tensor and is theoretically computed by a plane wave Eigenvalue solution. The stiffness parameter is considered as a state variable and predicted using the UKF. At first, the architecture of the inversion algorithm is verified with the FEM simulation data, as the true values are known in the case of numerical simulation. In this case, the accuracy in the estimation of the parameter is more than 97 %. The UKF is a data-driven hybrid technique that takes advantage of the data collected from a field experiment in conjunction with the physics-informed mathematical model. The prediction results obtained from the UKF technique are compared with the theoretical state parameters. The UKF, being a Bayesian filter, accounts for measurement uncertainties, thereby providing a confidence level on

the estimate to facilitate the decision-making process. It has been demonstrated through the experimental investigation that the velocity measurements are sufficient to estimate the parameter with an accuracy of more than 93 %. It is worth noting that the velocity of a wave in any direction can be extracted from the full-field transient images. However, the UKF algorithm needs limited experimental velocity information along the angular direction that may even be perturbed by measurement uncertainty/noise. Further, the proposed algorithm is generic that utilizes available physics-informed mathematical models and relevant experimental techniques with limited measurements. The compatibility of different experimental procedures and the suitability of non-linear systems within the UKF framework makes the proposed methodology robust, reliable and applicable in other real-life scenarios.

Declaration of Competing Interest

The authors declare that they have no known competing financial interests or personal relationships that could have appeared to influence the work reported in this paper.

Data availability

Data will be made available on request.

Acknowledgement:

Amit Shelke and Nur M. M. Kalimullah acknowledge Indian Space Research Organisation (ISRO) for supporting this work under grant number ISRO/RES/STC/IITG/2021-22. Anowarul Habib acknowledge the Research Council of Norway, International Partnerships for Excellent Education, Research and Innovation (INTPART) Project, under Grant 309802 and Cristin Project, Norway, ID: 2061348 (Habib) for supporting this work. The publication charges for this article have been funded by a grant from the publication fund of UiT, The Arctic University of Norway.

References:

[1] R.W. Boyd, Nonlinear optics, Academic press, 2020.
[2] R. Weis, T. Gaylord, Lithium niobate: summary of physical properties and crystal structure, Appl. Phys. A 37 (1985) 191–203.
[3] R. Geiss, S. Saravi, A. Sergeyev, S. Diziain, F. Setzpfandt, F. Schrempel, R. Grange, E.-B. Kley, A. Tünnermann, T. Pertsch, Fabrication of nanoscale lithium niobate waveguides for second-harmonic generation, Opt. Lett. 40 (2015) 2715–2718.
[4] M. Zhang, C. Wang, R. Cheng, A. Shams-Ansari, M. Lončar, Monolithic ultra-high-Q lithium niobate microring resonator, Optica 4 (2017) 1536–1537.
[5] J. Lin, Y. Xu, Z. Fang, M. Wang, J. Song, N. Wang, L. Qiao, W. Fang, Y. Cheng, Fabrication of high-Q lithium niobate microresonators using femtosecond laser micromachining, Sci. Rep. 5 (2015) 1–4.
[6] D. Pohl, M.R. Escalé, M. Madi, F. Kaufmann, P. Brotzer, A. Sergeyev, B. Guldimann, P. Giaccari, E. Alberti, U. Meier, An integrated broadband spectrometer on thin-film lithium niobate, Nat. Photonics 14 (2020) 24–29.
[7] C. Wang, M. Zhang, B. Stern, M. Lipson, M. Lončar, Nanophotonic lithium niobate electro-optic modulators, Opt. Express 26 (2018) 1547–1555.
[8] C. Wang, M. Zhang, X. Chen, M. Bertrand, A. Shams-Ansari, S. Chandrasekhar, P. Winzer, M. Lončar, Integrated lithium niobate electro-optic modulators operating at CMOS-compatible voltages, Nature 562 (2018) 101–104.
[9] C. Wang, X. Xiong, N. Andrade, V. Venkataraman, X.-F. Ren, G.-C. Guo, M. Lončar, Second harmonic generation in nano-structured thin-film lithium niobate waveguides, Opt. Express 25 (2017) 6963–6973.
[10] J. Zhao, M. Rüsing, U.A. Javid, J. Ling, M. Li, Q. Lin, S. Mookherjea, Shallow-etched thin-film lithium niobate waveguides for highly-efficient second-harmonic generation, Opt. Express 28 (2020) 19669–19682.
[11] J. Zhao, M. Rüsing, M. Roeper, L.M. Eng, S. Mookherjea, Poling thin-film x-cut lithium niobate for quasi-phase matching with sub-micrometer periodicity, J. Appl. Phys. 127 (2020), 193104.
[12] L. Chang, Y. Li, N. Volet, L. Wang, J. Peters, J.E. Bowers, Thin film wavelength converters for photonic integrated circuits, Optica 3 (2016) 531–535.
[13] A. Habib, A. Shelke, M. Pluta, T. Kundu, U. Pietsch, W. Grill, Imaging of acoustic waves in piezoelectric ceramics by coulomb coupling, Jpn. J. Appl. Phys. 51 (2012) 07GB05.
[14] A. Habib, U. Amjad, M. Pluta, U. Pietsch, W. Grill, Surface acoustic wave generation and detection by Coulomb excitation, in: Health Monitoring of Structural and Biological Systems 2010, International Society for Optics and Photonics, 2010, pp. 76501T.
[15] A. Shelke, A. Habib, U. Amjad, M. Pluta, T. Kundu, U. Pietsch, W. Grill, Metamorphosis of bulk waves to Lamb waves in anisotropic piezoelectric crystals, in: Health Monitoring of Structural and Biological Systems 2011, 2011, pp. 341–352.
[16] W. Han, X. Bu, M. Song, X. Huang, Research into a novel surface acoustic wave sensor signal-processing system based on compressive sensing and an observed-signal augmentation method based on secondary information prediction, Meas. Sci. Technol. 32 (2021), 075902.
[17] C.C. Ruppel, Acoustic wave filter technology–a review, IEEE Trans. Ultrason. Ferroelectr. Freq. Control 64 (2017) 1390–1400.
[18] W. Mortley, Improvements in or relating to wave energy delay cells, UK Patent 988102 (1962).
[19] R. Whatmore, P. Goddard, B. Tanner, G. Clark, Direct imaging of travelling Rayleigh waves by stroboscopic X-ray topography, Nature 299 (1982) 44–46.
[20] M. Foerster, N. Statuto, B. Casals, A. Hernández-Mínguez, S. Finizio, A. Mandziak, L. Aballe, J.M. Hernàndez Ferràs, F. Macia, Quantification of propagating and standing surface acoustic waves by stroboscopic X-ray photoemission electron microscopy, J. Synchrotron Radiat. 26 (2019) 184–193.
[21] T. Hesjedal, E. Chilla, H.J. Fröhlich, Scanning acoustic force microscope investigations of surface acoustic waves, Surf. Interface Anal. 25 (1997) 569–572.
[22] R. Vines, S.-I. Tamura, J. Wolfe, Surface acoustic wave focusing and induced Rayleigh waves, Phys. Rev. Lett. 74 (1995) 2729.
[23] D. Roshchupkin, M. Brunel, R. Tucoulou, E. Bigler, N. Sorokin, Reflection of surface acoustic waves on domain walls in a LiNbO3 crystal, Appl. Phys. Lett. 64 (1994) 164–165.
[24] W. Hamilton, M. Yethiraj, Effects of traveling surface acoustic waves on neutron Bragg scattering from perfect crystals, Phys. Rev. B 59 (1999) 3388.
[25] P. Hess, A.M. Lomonosov, Solitary surface acoustic waves and bulk solitons in nanosecond and picosecond laser ultrasonics, Ultrasonics 50 (2010) 167–171.
[26] C. Thomsen, J. Strait, Z. Vardeny, H.J. Maris, J. Tauc, J. Hauser, Coherent phonon generation and detection by picosecond light pulses, Phys. Rev. Lett. 53 (1984) 989.
[27] C. Thomsen, H.T. Grahn, H.J. Maris, J. Tauc, Surface generation and detection of phonons by picosecond light pulses, Phys. Rev. B 34 (1986) 4129.
[28] J.-I. Kushibiki, I. Takanaga, M. Arakawa, T. Sannomiya, Accurate measurements of the acoustical physical constants of LiNbO/sub 3/and LiTao/sub 3/single crystals, IEEE Trans. Ultrason. Ferroelectr. Freq. Control 46 (1999) 1315–1323.
[29] J.P. Wolfe, Imaging phonons: acoustic wave propagation in solids, Cambridge University Press, 2005.
[30] Y. Sugawara, O. Wright, O. Matsuda, M. Takigahira, Y. Tanaka, S. Tamura, V. Gusev, Watching ripples on crystals, Phys. Rev. Lett. 88 (2002), 185504.
[31] W. Grill, K. Hillmann, K.U. Würz, J. Wesner, Scanning ultrasonic microscopy with phase contrast, in: Advances in Acoustic Microscopy, Springer, 1996, pp. 167–218.
[32] B.A. Auld, Acoustic fields and waves in solids, John Wiley and Sons, New York, 1973.
[33] A. Every, M. Pluta, W. Grill, K. Würz, Progression from ballistic phonon focusing to internal diffraction of ultrasound in crystals, Physica Status Solidi (c) 1 (2004) 2951–2954.
[34] A. Habib, E. Twerdowski, M. von Buttlar, M. Pluta, M. Schmachtl, R. Wannemacher, W. Grill, Acoustic holography of piezoelectric materials by Coulomb excitation, in: Health Monitoring and Smart Nondestructive Evaluation of Structural and Biological Systems V, International Society for Optics and Photonics, 2006, pp. 61771A.
[35] D. Royer, E. Dieulesaint, Elastic waves in solids I: Free and guided propagation, Springer Science & Business Media, 1999.
[36] K. Gao, X. Liu, J. Xiong, L. Liang, Elastic parameter inversion of Longmaxi Formation shale based on the least squares method, Arab. J. Geosci. 14 (2021) 1–10.
[37] R. Cui, F.L. di Scalea, On the identification of the elastic properties of composites by ultrasonic guided waves and optimization algorithm, Compos. Struct. 223 (2019), 110969.
[38] K. Balasubramaniam, Inversion of the ply lay-up sequence for multi-layered fiber reinforced composite plates using genetic algorithm, Nondestructive Testing and Evaluation 15 (1998) 311–331.
[39] Q. Chen, K. Xu, D. Ta, High-resolution Lamb waves dispersion curves estimation and elastic property inversion, Ultrasonics 115 (2021), 106427.
[40] M. Rautela, S. Gopalakrishnan, K. Gopalakrishnan, Y. Deng, Ultrasonic guided waves based identification of elastic properties using 1d-convolutional neural networks, in: 2020 IEEE International Conference on Prognostics and Health Management (ICPHM), IEEE, 2020, pp. 1–7.
[41] K. Gopalakrishnan, M. Rautela, Y. Deng, Deep learning based identification of elastic properties using ultrasonic guided waves, in: European Workshop on Structural Health Monitoring, Springer, 2020, pp. 77–90.
[42] T. Hajzargerbashi, T. Kundu, S. Bland, An improved algorithm for detecting point of impact in anisotropic inhomogeneous plates, Ultrasonics 51 (2011) 317–324.
[43] T. Kundu, H. Nakatani, N. Takeda, Acoustic source localization in anisotropic plates, Ultrasonics 52 (2012) 740–746.
[44] A. Shelke, T. Kundu, U. Amjad, K. Hahn, W. Grill, Mode-selective excitation and detection of ultrasonic guided waves for delamination detection in laminated aluminum plates, IEEE Trans. Ultrason. Ferroelectr. Freq. Control 58 (2011) 567–577.
[45] E.D. Niri, A. Farhidzadeh, S. Salamone, Nonlinear Kalman Filtering for acoustic emission source localization in anisotropic panels, Ultrasonics 54 (2014) 486–501.

[46] J. Ding, J. Chen, J. Lin, L. Wan, Particle filtering based parameter estimation for systems with output-error type model structures, J. Franklin Inst. 356 (2019) 5521–5540.
[47] X. Jia, O. Sedehi, C. Papadimitriou, L.S. Katafygiotis, B. Moaveni, Hierarchical Bayesian modeling framework for model updating and robust predictions in structural dynamics using modal features, Mech. Syst. Sig. Process. 170 (2022), 108784.
[48] R. Madankan, P. Singla, T. Singh, P.D. Scott, Polynomial-chaos-based Bayesian approach for state and parameter estimations, J. Guid. Control Dynam. 36 (2013) 1058–1074.
[49] J.L. Crassidis, J.L. Junkins, Optimal estimation of dynamic systems, Chapman & Hall/CRC Applied Mathematics & Non-linear Science, Boca Raton, 2004.
[50] S. Thrun, Probabilistic robotics, Commun. ACM 45 (2002) 52–57.
[51] V. Agarwal, A. Shelke, B. Ahluwalia, F. Melandsø, T. Kundu, A. Habib, Damage localization in piezo-ceramic using ultrasonic waves excited by dual point contact excitation and detection scheme, Ultrasonics 108 (2020), 106113.
[52] N.M.M. Kalimullah, A. Shelke, A. Habib, Multiresolution Dynamic Mode Decomposition (mrDMD) of Elastic Waves for Damage Localisation in Piezoelectric Ceramic, IEEE Access 9 (2021) 120512–120524.
[53] A. Habib, A. Shelke, M. Pluta, U. Pietsch, T. Kundu, W. Grill, Scattering and attenuation of surface acoustic waves and surface skimming longitudinal polarized bulk waves imaged by Coulomb coupling, in: AIP Conference Proceedings, American Institute of Physics, 2012, pp. 247–250.
[54] F.I. Fedorov, Theory of elastic waves in crystals, Springer Science & Business Media, 1968.
[55] S. Särkkä, Bayesian filtering and smoothing, Cambridge University Press, 2013.
[56] G. Welch, G. Bishop, An introduction to the Kalman filter, (1995).
[57] E.A. Wan, R. Van Der Merwe, The unscented Kalman filter for nonlinear estimation, in: Proceedings of the IEEE 2000 Adaptive Systems for Signal Processing, Communications, and Control Symposium (Cat. No. 00EX373), Ieee, 2000, pp. 153-158.
[58] S.J. Julier, J.K. Uhlmann, H.F. Durrant-Whyte, A new approach for filtering nonlinear systems, in: Proceedings of 1995 American Control Conference-ACC'95, IEEE, 1995, pp. 1628-1632.